Contents lists available at ScienceDirect

Bioactive Materials

journal homepage: www.keaipublishing.com/en/journals/bioactive-materials

A DNA tetrahedron-based nanosuit for efficient delivery of amifostine and multi-organ radioprotection

Yuting Yang [a,b], Jinlong Yang [d], Jianwei Zhu [e], Xingyu Chen [a,b], Li Zhou [f], Wenjuan Ma [a,b,**], Yunfeng Lin [a,b,c,*]

[a] State Key Laboratory of Oral Diseases, National Center for Stomatology, National Clinical Research Center for Oral Diseases, West China Hospital of Stomatology, Sichuan University, Chengdu, Sichuan, 610041, PR China
[b] Sichuan Provincial Engineering Research Center of Oral Biomaterials, Chengdu, Sichuan, 610041, PR China
[c] National Center for Translational Medicine, Shanghai Jiao Tong University, Shanghai, 200240, PR China
[d] Department of Neurosurgery of West China Hospital, Sichuan University, Chengdu, 610041, PR China
[e] Department of Neurosurgery, Sichuan Provincial People's Hospital, University of Electronic Science and Technology of China, Chengdu, 611731, PR China
[f] Histology and Imaging Platform, Core Facility of West China Hospital, Sichuan University, Chengdu, 610041, PR China

ARTICLE INFO

ABSTRACT

Unnecessary exposure to ionizing radiation (IR) often causes acute and chronic oxidative damages to normal cells and organs, leading to serious physiological and even life-threatening consequences. Amifostine (AMF) is a validated radioprotectant extensively applied in radiation and chemotherapy medicine, but the short half-life limits its bioavailability and clinical applications, remaining as a great challenge to be addressed. DNA-assembled nanostructures especially the tetrahedral framework nucleic acids (tFNAs) are promising nano-carriers with preeminent biosafety, low biotoxicity, and high transport efficiency. The tFNAs also have a relative long-term maintenance for structural stability and excellent endocytosis capacity. We therefore synthesized a tFNA-based delivery system of AMF for multi-organ radioprotection (tFNAs@AMF, also termed nanosuit). By establishing the mice models of accidental total body irradiation (TBI) and radiotherapy model of Lewis lung cancer, we demonstrated that the nanosuit could shield normal cells from IR-induced DNA damage by regulating the molecular biomarkers of anti-apoptosis and anti-oxidative stress. In the accidental total body irradiation (TBI) mice model, the nanosuit pretreated mice exhibited satisfactory alteration of superoxide dismutase (SOD) activities and malondialdehyde (MDA) contents, and functional recovery of hematopoietic system, reducing IR-induced pathological damages of multi-organ and safeguarding mice from lethal radiation. More importantly, the nanosuit showed a selective radioprotection of the normal organs without interferences of tumor control in the radiotherapy model of Lewis lung cancer. Based on a conveniently available DNA tetrahedron-based nanocarrier, this work presents a high-efficiency delivery system of AMF with the prolonged half-life and enhanced radio-protection for multi-organs. Such nanosuit pioneers a promising strategy with great clinical translation potential for radioactivity protection.

1. Introduction

The extensive application of ionizing radiation (IR) in industry, agriculture, and medicine increases the risk of radiation exposure, including accidental total body irradiation (TBI) [1,2]. Radiotherapy, for example, is now a mainstay treatment for malignant tumors in clinics and for a better tumor treatment, over half of cancer patients receive high-energy radiotherapy to kills cancer cells by damaging their DNA and inducing cellular apoptosis [3,4]. When exposed to radiation, large amounts of oxygen free radicals are rapidly produced, such as reactive

oxygen species (ROS), provoking a state of oxidative stress [5]. The generated oxygen free radicals can react with DNA and RNA in normal cells and organs, and eventually causes structural and functional changes. However, excessive and unexpected radiation inevitably brings about deleterious consequences and causes terrible diseases, such as acute radiation syndrome (ARS), chronic radiation syndrome (CRS), or even cancers, whilst radiation to the lower abdomen or pelvis is very likely to affect fertility [4,6–8].

Undesirable hazards to healthy tissues nearby could easily be caused by radiotherapy, and early effects include skin and mucosal diseases might precede to the anti-tumor effects after just few days or weeks of such treatment. Long-term toxicity such as chronic inflammation and tissue fibrosis might also emerge after long with odds for secondary cancers. There are also pathways where the body is functioning for self-repairing. Ataxia-telangiectasia mutated (ATM), Rad3-related (ATR), and DNA dependent protein kinase catalytic subunit (DNA PKcs) are significant switch molecules that initially regulate the DNA damage response (DDR) signaling network [9,10]. After radiation, ATM catalyzes the phosphorylation of H2A histone family member X (H2A.X) on Ser139 to generate the phosphorylated form γ-H2A.X, and various substrate proteins including nuclear transcription factor p53, v-myc myelocytomatosis viral oncogene homolog (c-myc), checkpoint kinase 1 (Chk1) and checkpoint kinase 2 (Chk2). These signal transduction pathways are bound up with cellular responses against radiation-related processes, including oxidative stress, DNA damage and cell apoptosis. However, when such self-repairing process is overwhelmed, massive cells in radiosensitive tissues will lose and severe cellular and tissue damage then will show up [11–13]. That says, while the balance between benefits and harms regarding radiotherapy should always be a consideration in clinical decisions, it might be better to develop effective radioprotection to minimize the side effects while maximize the benefit.

While capability of previously developed radioprotections including taminothiol compounds, hormones, cytokines and receptor agonists to selectively shield healthy tissues from high-energy radiations has rarely been proved [14–16]. Amifostine (AMF) is a validated radioprotectant extensively applied in radiation medicine approved by the U.S. Food and Drug Administration (FDA). AMF exhibits selective radioprotection and chemoprotection of normal tissues but not tumors, due to that normal tissues possess higher activities of alkaline phosphatase (ALP) than tumors, which could transfer AMF into the active form of WR-1065 and disulfide WR-33278. The WR-1065 is the major mediator for subsequent radiation protection [17–20]. However, the short half-life of AMF means that a high dosage is usually adopted to function against radiation, which may bring systemic toxicity and complications, such as hypotension, nausea, and vomiting. Conversely, a safe concentration range is difficult to achieve satisfactory radioprotection [21,22]. Therefore, extending the half-life and increasing the bioavailability of AMF remains a challenge to be addressed before wide application for radioprotection, and it is precisely the scientific issue currently discussed in this paper.

Recently, DNA-assembled nanostructures receive growing interests in tissue engineering and drug delivery. The size, shape, and spatial structure of these nucleic-acid nanomaterials can be precisely designed as promising nanocarriers with excellent biocompatibility, low biotoxicity, and high cargo transport efficiency [23,24]. Among them, tetrahedral framework nucleic acids (tFNAs), typical multi-arm DNA tiles for three-dimensional polyhedron, have exhibited overwhelming superiority as drug carriers in many biomedical applications [25–35]. The strengths of tFNAs include: (i) they are easy edited and well functionalized, allowing for the attachment of oligonucleotides, peptides, and various small molecular weights; (ii) relatively long-term maintenance of its structural stability and excellent endocytosis capacity to penetrate cells and tissues endows it extraordinary cellular membrane affinity, assuring biocompatibility, binding, and endocytosis [36]; and (iii) tFNAs are also reported to promote cell survival, alleviate progressive inflammation, and reduce oxidative stress response, showing great potentials in regenerative medicine [37–39]. Thus, to obtain

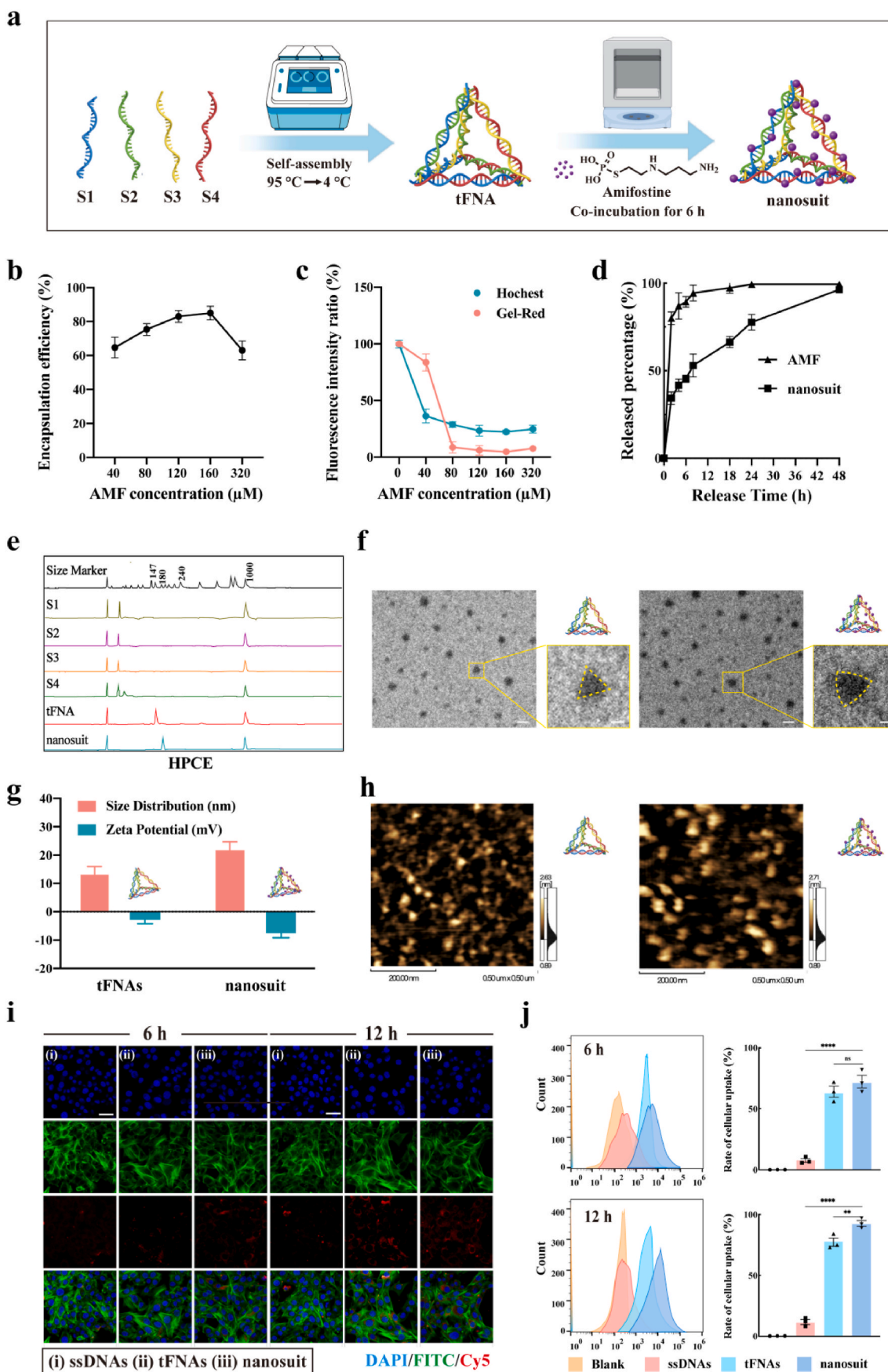insights into the potentials of tFNAs on the delivery of AMF is sparked.

Herein, a tFNA-based delivery system for AMF was introduced as an original protectant (tFNAs@AMF), which acts as the "nanosuit" for securely safeguarding organisms from IR, just like wearing a nano-sized radiation protective suit for normal cells. The nanosuit could protect normal cells against IR-induced DNA damage, superior to pure AMF. The regulation of ATM/ATR signal pathways laid a theoretical basis for the potential efficacy. Both in accidental TBI model and radiotherapy model of Lewis lung cancer, the data indicated that the nanosuit could shield mice from a lethal dose of IR, and effectively accelerate hematopoietic recovery and prevent IR-induced multi-organ damage. Moreover, the pretreatment of the nanosuit won't interfere treatment efficiency of radiotherapy for tumors. Inspired by equipping normal cells with radioprotective armor, our findings propose a DNA tetrahedron-based nanosuit for efficient delivery of AMF and multi-organ radioprotection, which addresses the challenge of short half-life of the *in-vivo* administration of free AMF.

2. Results and discussion

2.1. Synthesis, characterization, and cellular internalization of the nanosuit

The schematic illustration in Fig. 1a showed the synthesis procedure of nanosuit by a two-step method. First, four specific single-stranded DNAs (ssDNAs, Table S1, Supporting Information) were assembled into tFNAs. Secondly, corresponding concentrations of AMF (40, 80, 120, 160, and 320 μM) were respectively mixed with tFNAs by co-incubation. According to the standard curve of AMF (Fig. S1, Supporting Information), the encapsulation efficiency was calculated. The encapsulation efficiency elevated with increasing AMF concentration, reached its peak and then dropped (Fig. 1b). To further verify the successful synthesis of the nanosuit, a fluorescence spectrophotometer was applied to determine the fluorescence spectra of Gel-Red and Hochest 33342. When nanosuit was incubated with Gel-Red or Hochest33342, the fluorescence intensity became weaker with increasing AMF concentration (Fig. 1c), suggesting the groove binding and intercalative binding of AMF to the tFNAs. Fig. 1d showed the release curve in PBS. AMF alone was quickly released from dialysis in PBS, while the release of AMF from nanosuit was characterized by a gradual pattern. Furthermore, the release behavior of AMF and nanosuit in fetal bovine serum (FBS) is depicted in Fig. S2, Supporting Information. AMF from the nanosuit exhibited a relatively slow release. This sustained release pattern would be helpful for the fully utilization of AMF. The high performance capillary electrophoresis (HPCE) showed that the molecular weight of tFNAs was nearly 180 bp, and that of nanosuit was more than 180 bp; the difference might suggest that the AMF was loaded to tFNA (Fig. 1e). Moreover, the ζ-potential of tFNA and nanosuit was negative, and the value of them was -2.87 ± 0.78 mV and -7.53 ± 0.95 mV, respectively (Fig. 1e and Fig. S3, Supporting Information). Additionally, the particle sizes of tFNAs and the nanosuit were observed by dynamic light scattering (DLS) and transmission electron microscopy (TEM). Outcomes (Fig. 1f and g) revealed that the size of tFNA was approximately 10 nm while that of nanosuit was larger than tFNAs. Moreover, TEM results showed that tFNA was a tetrahedral structure while nanosuit revealed around triangular shape. Atomic force microscopy (AFM) also confirmed the dimensions (Fig. 1h). These results verified and characterized the synthesized nanosuit, suggesting that tFNAs might be a favorable carrier for small molecules.

Prior to assess radioprotective efficacy of the nanosuit *in vitro*, confocal fluorescence microscopy and flow cytometric analysis were employed to monitor cellular internalization. The fluorescence of Cy5 labeled S1 was employed to visualize the entry of materials. BALB/3T3 clone A31 mouse fibroblasts (A31) cells were exposed to Cy5-modified ssDNAs, tFNAs or the nanosuit for 6 and 12 h. In Fig. 1i, the fluorescence intensities of Cy5 in cells exposed to tFNAs or the nanosuit were

Fig. 1. Synthesis and characterization of nanosuit. (a) Schematic illustration showing the synthesis procedures of nanosuit. (b) The encapsulation efficiency of AMF in the tFNAs was examined using HPLC (n = 3). (c) The fluorescence intensity ratios of Gel-Red and Hocheset 33342 of nanosuit with the presence of different concentrations of AMF (n = 3). (d) *In vitro* release assay of AMF and nanosuit in PBS (pH 7.4, 37 °C). (e) The molecular weights of tFNAs and nanosuit analyzed by HPCE. (f) TEM images of tFNAs and nanosuit (Scale bars are 25 nm; scale bars in magnification images are 5 nm). (g) The particle size and ζ-potential value of tFNA and nanosuit (n = 3). (h) AFM image illustrates size and morphology of tFNAs and nanosuit. (i) Representative fluorescence images of Cy5 showing the cellular internalization of ssDNAs, tFNAs and nanosuit at 6 h and 12 h (Scale bars are 50 μm). (j) Cellular internalization of ssDNAs, tFNAs and nanosuit at 6 h and 12 h via flow cytometry and its quantitative analysis (n = 3). Error bars denote mean ± SEM. Statistical analysis: **P < 0.01, ****P < 0.0001; ns, not statistically significant.

both stronger than ssDNAs, and more nanosuits were internalized by A31 cells at 12 h than that of 6 h. The result of flow cytometry further verified this phenomenon of confocal images in cell internalization of ssDNAs, tFNAs, or nanosuit (Fig. 1j).

2.2. Protective efficacy of nanosuit on intracellular DNA against IR-induced damages

The schematic illustration in Fig. 2a showed that the nanosuit protected DNA against IR-induced damage *in vitro*. We first evaluated the effects of the nanosuit on the cell survival under different doses of IR. We found that the nanosuit could rescue IR-induced cell death, compared with AMF and tFNAs pretreated groups (Fig. 2b), indicating the powerful protection of the nanosuit against IR. The dose of 6 Gy was selected for use in subsequent experiments [40]. As a by-product of biological aerobic metabolism, ROS possesses strong chemical reactivity and affects a series of signal transduction pathways. Stimulated by radiation exposure, ROS will increase sharply, triggering cellular oxidative stress and reaction with intracellular DNA. As shown in Fig. 2c and g, the nanosuit pretreatment lowered the level of IR-induced intracellular ROS to a certain extent, indicating that the radioprotective capacity of the nanosuit was related to its effective radical scavenging activity.

One of the hallmarks of IR-induced cellular damage is uncontrolled DNA breakage, accompanied by cell senescence and arrest. According to the principle of DNA damage, the detection can be based on changes in physico-chemical properties of damaged DNA, such as the comet assay, also named as single cell gel electrophoresis (SCGE). Images showed that negligible DNA damages were detected in normal cells, while cell tails representing DNA damages were readily identified under IR (Fig. 2d). In contrast to the IR group, cell tails of those pretreated with the nanosuit presented distinct recovery. Quantitative analysis of tail DNA (Fig. 2g) suggested that cells pretreated with the nanosuit recovered to an appreciable degree (9.35 ± 3.23 %), as compared to cells pretreated with simplex AMF (33.27 ± 7.14 %) or tFNAs (50.16 ± 4.73 %), consistent with changes in tail moment and tail length (Fig. S4, Supporting Information). As a product forming from DNA damage, γ-H2A.X can be another key biomarker of IR-damaged DNA. H2A.X participated in nucleosomal organization of chromatin and is rapidly phosphorylated in the presence of IR, producing a marked effect in reflecting the extent of DNA damage and repair. In this study, a stronger fluorescence signal of γ-H2A.X was identifiable in the IR group compared with unirradiated group, which indicated that the integrity of DNA was disrupted (Fig. 2e). The level of γ-H2A.X in the nanosuit group was lower compared with other groups, demonstrating that the nanosuit pretreatment alleviated DNA damage. In addition, as a 450-kDa kinase indispensable for DNA damage response, immunofluorescence on DNA PKcs was performed to visualize the extent of DNA damage (Fig. 2f). A weaker DNA PKcs intensity was observed in the nanosuit pretreatment group than other groups, indicating a novel protective role of the nanosuit on DNA against IR.

2.3. Mechanism and signal pathway underlying the protective effects of nanosuit

In radiosensitive tissues, ATM/ATR signaling pathway plays a vital role in the process of DNA damage, oxidative stress and cell apoptosis. We hypothesized that nanosuit exerted a protective effect by blocking the ATM/ATR pathway and regulating downstream pathways, as shown in Fig. 3a. The outcomes of Western blot revealed that the expression of ATM, ATR, C-myc, Chk1, Chk2, and p53 was evidently decreased with pretreatment of the nanosuit, while at a high expression in IR group, indicating the nanosuit could suppress the abnormal activation of ATM/ATR signaling pathway (Fig. 3d–e). And the downstream pathways were also examined. The fluorescence intensity analysis of Caspase-3, Bcl-2, Bax, and Cytochrome *c* revealed that the nanosuit pretreatment significantly decreased the fluorescence intensities of Caspase-3, Bax, and Cytochrome *c* while evidently strengthened expression of Bcl-2 (Fig. 3b, Figs. S5 and S6, Supporting Information). The result was further confirmed by TUNEL assay. Nanosuit pretreatment remarkably reduced the IR-induced TUNEL positive cells as compared to only AMF or tFNAs pretreated group (Fig. 3c and Fig. S7, Supporting Information). In addition, the representative Western blot images and semi-quantitative analysis in Fig. 3f–g were consistent with the fluorescence results as described above.

Herein, we could find out that the ability of regulating the ATM/ATR signaling pathway made the nanosuit an effective radioprotectant for protecting cells against IR exposure. Blockade of ATM/ATR pathway occurred first and the downstream pathways of anti-apoptosis and anti-oxidative stress were then activated. Thus, the separation of Bcl-xl and Bcl-2 from Bad enabled dissociative Bcl-2 to function, along with low expression of Bax and decline in mitochondrial membrane permeability, ultimately suppressing release of Cytochrome *c* and excessive activation of Caspase-3 [41]. The oxidative stress was also suppressed, thus altering the SOD activities and MDA contents and mitigating IR-induced ROS.

2.4. Prolonged mice survival and promoted hematopoietic recovery in accidental TBI model

To investigate the systemic radioprotective effects of the nanosuit, BALB/c mice exposed to TBI were introduced in subsequent experiments. The animal experimental design for the radioprotection assay was shown in Fig. 4a. Theoretically, IR-induced injuries aggravate within 7–10 days and plenty of mice even tend to die. Then, the tissue damages were mitigated gradually over 30 days. Therefore, we monitored the effects of the nanosuit pretreatment on survival after lethal TBI (6.5 Gy) within 30 days [41]. The results (Fig. 4b and Fig. S8, Supporting Information) demonstrated that the 30-day survival percentage was 0 % in the tFNAs + IR group with the survival time of 9.8 ± 1.9 days, and 20 % in the AMF + IR group with the survival time of 15.4 ± 7.3 days, and 70 % in the nanosuit + IR group with the survival time of 25.1 ± 7.2 days, compared with 100 % mortality in mice receiving IR alone. Taken together, the nanosuit efficaciously enhanced survival of mice suffering from a lethal dose of TBI, and thereby reduced radiation toxicity and safeguarded mice from lethal ARS.

The Cy5 was labeled to track the distribution of materials in *ex vivo* imaging system at different times post injection of tFNAs or the nanosuit (15, 30, 60, and 120 min). The image (Fig. 4c) indicated that materials were distributed in the major organs and progressively accumulated and cleared in kidney and liver. Moreover, the administration of nanosuit showed delayed renal clearance and prolonged distribution in major organs, which indicated that the AMF loading could alter the accumulation time of tFNAs and AMF (Fig. S9, Supporting Information). The optimized pharmacokinetic profiles of the nanosuit would act more efficient IR protection for normal organs than AMF, which present great potential in clinical applications. In order to detect the distribution of
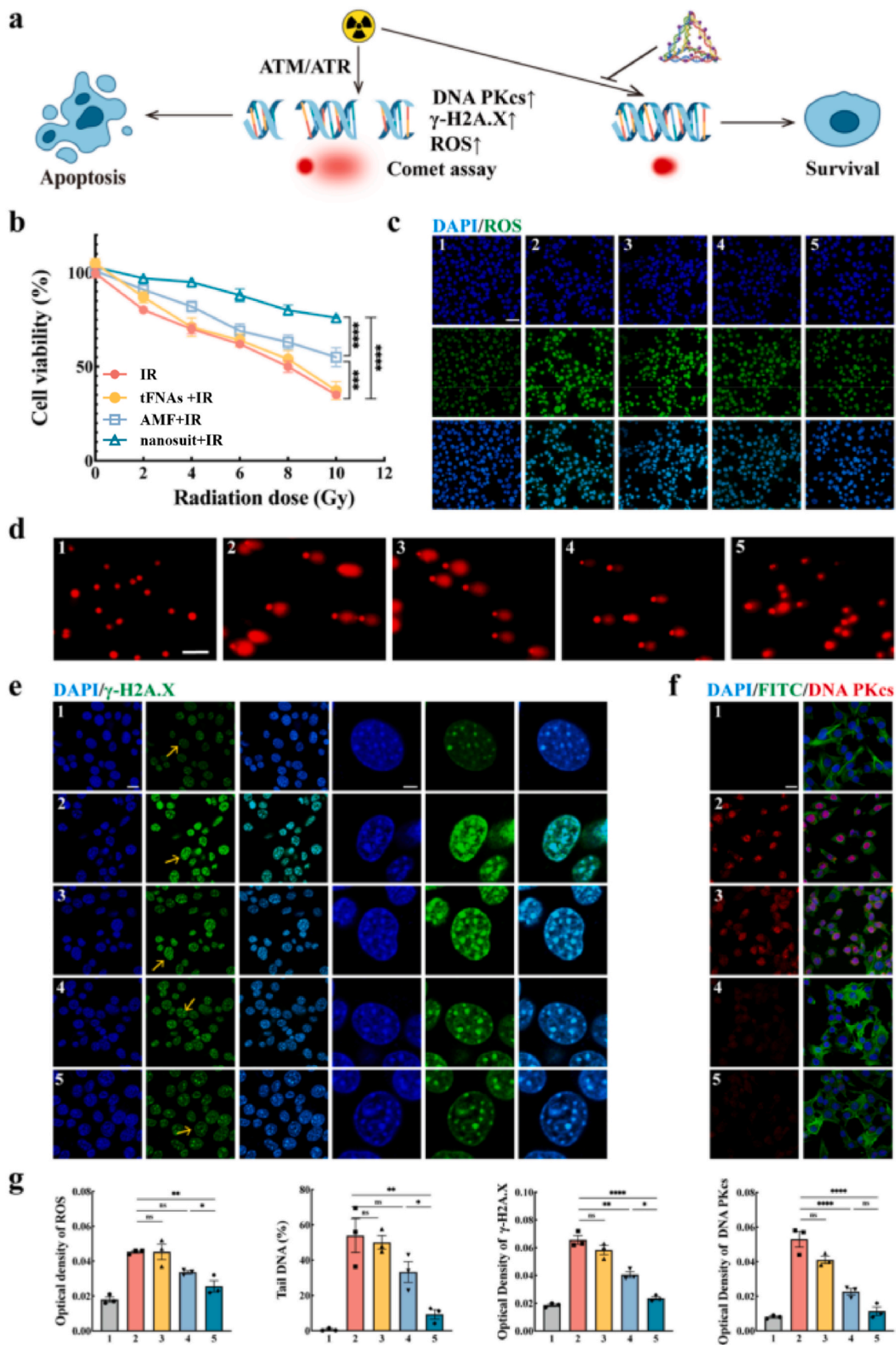
(caption on next page)

Fig. 2. The protective effects of nanosuit on DNA against IR-induced damage *in vitro*. (a) Schematic illustration of nanosuit protecting DNA against IR-induced damage. (b) Cell viabilities of A31 cells under different doses of IR (0, 2, 4, 6, 8, and 10 Gy) with pretreatment of tFNAs, AMF, or nanosuit (n = 5). (c) Representative fluorescence images of ROS in cells exposed to 6 Gy with pretreatment of tFNAs, AMF, or nanosuit (Scale bars are 50 μm). (d) Representative comet images of A31 cells exposed to 6 Gy with pretreatment of tFNAs, AMF, or nanosuit (Scale bars are 100 μm). (e) Representative immunofluorescence images of γ-H2A.X in cells exposed to 6 Gy with pretreatment of tFNAs, AMF, or nanosuit (Scale bars are 20 μm, and scale bars in magnification images are 5 μm). (f) Representative immunofluorescence images of DNA PKcs in cells exposed to 6 Gy with pretreatment of tFNAs, AMF, or nanosuit (Scale bars are 20 μm). (g) Semi-quantitative analysis of (c–f) (n = 3). Error bars denote mean ± SEM. Statistical analysis: *$P < 0.05$, **$P < 0.01$, and ****$P < 0.0001$; ns, not statistically significant. 1, Control; 2, IR; 3, tFNAs + IR; 4, AMF + IR; 5, nanosuit + IR.

nanosuit for a longer period, the *ex vivo* images of major organs after 3 times adiministration (qd) and a single dose from 15 min to 24 h are presented in Figs. S10 and S11, Supporting Information. The data indicated that the group with the most abundant material distribution is the mice received 3 times adiministration (qd) and detected after 15 min at the end of administration on day 3. And organ distribution gradually decreased as the administration time increased from 15 min to 24 h. Moreover, plasma pharmacokinetics of tFNAs, nanosuit, and free AMF were added to detect the metabolism in blood (Fig. S12, Supporting Information). The data showed that AMF was half cleared at approximately 0.5 h and completely degraded after 6 h, while the half-life of nanosuit was around 7 h. The clearance rate of nanosuit was slower than that of AMF, which suggested that tFNAs effectively suppressed the clearance rate of AMF. From the above, we concluded that nanosuit displayed good bioavailability *in vivo*.

Hematopoietic system is a highly sensitive tissue to IR, and bone marrow (BM) suppression is the major manifestation of IR-induced hematopoietic injury, a crucial factor of death for victims of radiation exposure, inducing the depletion of peripheral blood cell lineages [42, 43]. Thus, peripheral blood cell counts were used to estimate the radioprotective effects of the nanosuit. At the sub-lethal dose (5 Gy) of TBI, all three types of hemocytes showed an accentuated decrease in cell counts. White blood cell (WBC) counts significantly dropped in irradiated mice and this phenomenon was most pronounced at 7 days post-TBI (Fig. 4d). By contrast, pre-treatment with the nanosuit markedly elevated the WBC counts at 1 or 7 days post-TBI, which were nearly 2–3 folds higher than those in IR group. Furthermore, the nanosuit accelerated the renewal of WBC at 30 days post-TBI, almost to a normal state. As hypothesized, the change trends of red blood cell (RBC) and platelet (PLT) were the same as WBC, but more moderate (Fig. S13, Supporting Information). As Fig. 4e shown, at 1 and 7 days post-TBI, the relative amount of total DNA in marrow cells was drastically decreased to 0.461 ± 0.103 and 0.446 ± 0.071 compared with healthy mice. Instead, the relative content of total DNA in the nanosuit + IR group decreased to a higher value of 0.742 ± 0.066 at 1 day and rose to 0.905 ± 0.103 at 7 days, almost recovered to the healthy value. In addition, as shown in Fig. 4f, bone marrow cells in medullary cavity almost disappeared but RBCs were saturated at 7 days post-TBI. The nanosuit pretreatment largely mitigated the IR-induced BM suppression and hemorrhage, the same as bone marrow mononuclear cells (BM-MNCs) counts (Fig. S14, Supporting Information). Up until 30 days, BM cell composition was almost restored to a healthy level nearly that in control group. Furthermore, the nanosuit markedly decreased the TUNEL positive cells in femur, compared with pure AMF or tFNAs pretreated group (Fig. 4g and h). The apoptosis markers in bone marrow were evaluated and results were consistent with the *in vitro* experiments (Fig. S15, Supporting Information). These data illustrated that the pretreatment of the nanosuit could protect hematopoietic system and accelerate recovery of hematopoietic function by alleviating DNA damages induced by high-energy radiations.

2.5. Nanosuit prevented IR-induced multi-organ damage by restoring SOD activities and suppressing MDA contents

The radioprotective efficacy of the nanosuit in various organs (thymus gland, spleen, liver, testis, small intestine, lung, kidney, and oarium) was also examined (Fig. 5a). As optical micrographs of the thymus and spleen showed (Fig. 5b and c), apparent atrophy and structural damage were observed after IR exposure. However, the spleen atrophy and thymus atrophy in mice could be significantly abated by the nanosuit, as well as the improvement of thymus index and spleen index (Fig. 5i). Additionally, the liver in IR group exhibited hepatocytes degeneration and necrosis, with nuclear enrichment and fragmentation, while the nanosuit pretreatment improved hepatocyte morphology (Fig. 5d). The liver-function tests with alanine transaminase (ALT) and aspartate transaminase (AST) were consistent with pathological findings (Fig. S16, Supporting Information). Given that testis is one of the most highly sensitive tissues to radiation, pathohistological examination of it was performed (Fig. 5e). The irradiated mice exhibited evident degeneration and decline in number of spermatogenic cells in the seminiferous tubule. The morphology of testes almost returned to normal with the nanosuit pretreatment. The small intestine is also one of the most sensitive organs to IR [44]. Small intestine of irradiated mice showed obvious pathohistological injuries involving extensive villous atrophy, loose arrangement and damaged intestinal mucosa with a decrease in number of intestinal crypt cells (Fig. 5f). But there were no evident retarded regeneration and crypt abnormalities in the nanosuit + IR group, with villi remaining long and intact. Other organs including lung, kidney and oarium also presented moderate lesions under radiation while changes in the nanosuit pre-treated mice could be observed (Fig. S17, Supporting Information). The curves of body weight changes were consistent with these pathological results (Fig. S18, Supporting Information). These data demonstrated that the nanosuit preserved survival of major organs and promoted recovery from exposure to IR. For further detect whether the nansuit could act the protection after the occurrence of IR, more experiments were conducted (Fig. S19, Supporting Information). The experimental data demonstrated that post-radiation administration of nanosuit was far less effective than pretreatment, both in terms of mortality and the protection of vital organs (Figs. S20 and S21, Supporting Information). Thus, prophylactic application of nanosuit is more recommended.

To understand the underlying protection mechanism of nanosuit *in vivo*, superoxide dismutase (SOD) and malondialdehyde (MDA), which mediated oxidative stress response, were examined in plasma, hematopoietic tissue, spleen, liver, testis, and small intestine at 7 days post-sublethal TBI. SOD constitutes the first line of defense against abiotic stress-induced ROS as well as its reaction products [45]. In contrast, MDA is an end-product of membrane lipid peroxidation, and its contents indicates the severity of damages caused by radiation [46]. The result of Fig. 5g–h showed SOD activities and MDA contents of plasma and BM-MNCs at 7 days post-TBI. Upon exposure to IR, SOD activities notably decreased, whereas the nanosuit pretreatment exhibited robust recoveries, elucidating the ability to promote ROS clearance. Meanwhile, the MDA contents in the nanosuit + IR group was significant below the threshold value of non-pretreated mice. Similarly, as shown in Fig. 5j–m, exposure to IR also caused reduced SOD activities and elevated MDA contents in spleen, liver, testis, and small intestine. On the contrary, the nanosuit pretreatment significantly decelerated this trend in these organs, with some almost comparable to those of unirradiated mice. Collectively, the nanosuit could help to remove undesirable hazardous ROS in the body, and thereby avoid consumption of substantial SOD and producing excess MDA. As such, as the nanosuit with potencies against oxidative stress circulated into blood, they functioned by restoring SOD activities and suppressing MDA contents as free radical scavengers.
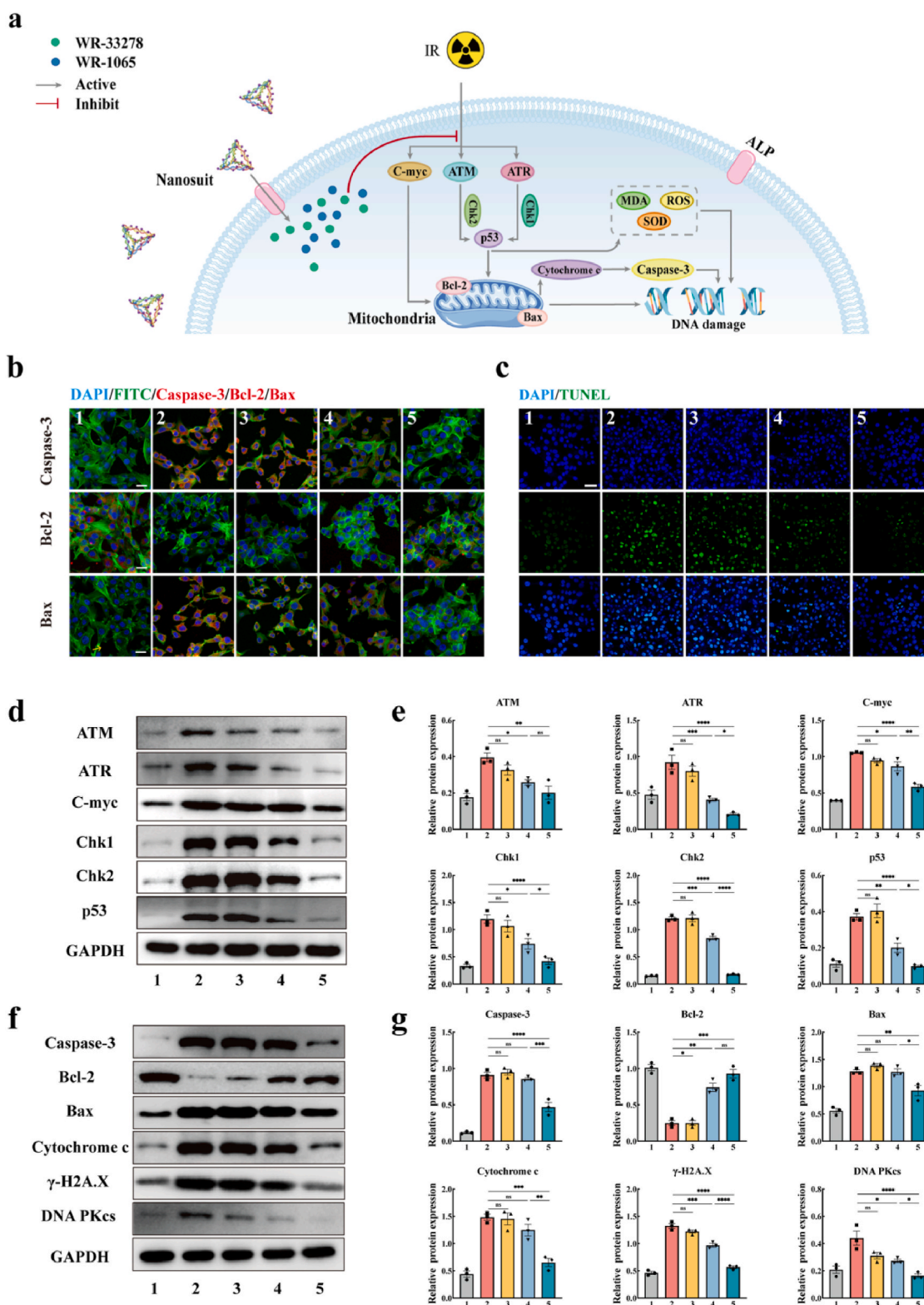
Fig. 3. The mechanism and signal pathway for the protective effects of nanosuit. (a) Schematic illustration of regulation mechanism and signal pathway of radiation protection *in vitro*. (b) Representative fluorescence images of Caspase-3, Bcl-2, and Bax in cells exposed to 6 Gy with pretreatment of tFNAs, AMF, or nanosuit (Scale bars are 20 μm). (c) Representative TUNEL staining images of A31 cells exposed to 6 Gy with pretreatment of tFNAs, AMF, or nanosuit (Scale bars are 50 μm). (d) Representative Western blot images showing the expression levels of ATM, ATR, C-myc, Chk1, Chk2, and p53. (e) Semi-quantitative analysis of the expression of ATM, ATR, C-myc, Chk1, Chk2, and p53 (n = 3). (f) Representative Western blot images showing the expression levels of Caspase-3, Bcl-2, Bax, Cytochrome *c*, γ-H2A. X, and DNA PKcs. (g) Semi-quantitative analysis of the expression of Caspase-3, Bcl-2, Bax, Cytochrome *c*, γ-H2A.X, and DNA PKcs (n = 3). Error bars denote mean ± SEM. Statistical analysis: *P < 0.05, **P < 0.01, ***P < 0.001, and ****P < 0.0001; ns, not statistically significant. 1, Control; 2, IR; 3, tFNAs + IR; 4, AMF + IR; 5, nanosuit + IR.
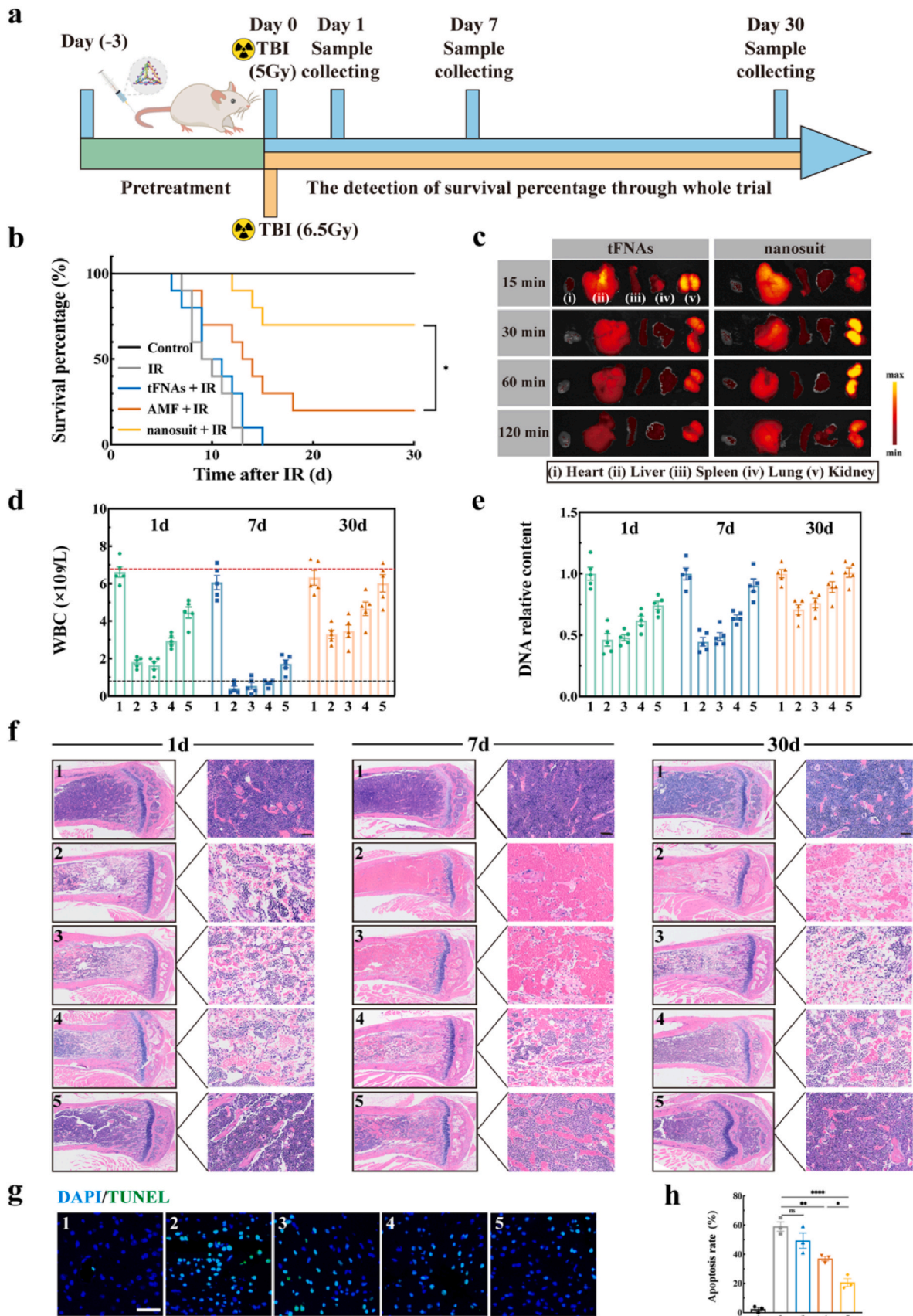
(caption on next page)

Fig. 4. Nanosuit enhanced mice survival and promoted hematopoietic recovery in accidental TBI model. (a) A schematic drawing of the experimental design for accidental TBI protection assays. (b) Survival analysis using Kaplan-Meier methods indicated the 30-day survival percentage of BALB/C mice exposed to 6.5 Gy TBI with pretreatment of tFNAs, AMF, or nanosuit. (n = 10). (c) Representative *ex vivo* images of major organs derived from mice at different times post injection of tFNAs or nanosuit (15, 30, 60, and 120 min). (d) Hematological parameter of WBC from mice at 1, 7, and 30 days post 5 Gy TBI with pretreatment of tFNAs, AMF, or nanosuit (n = 5). The blood test index falling between the black and the red dashed lines was considered normal. (e) DNA damages of mice at 1, 7, and 30 days post 5 Gy TBI with pretreatment of tFNAs, AMF, or nanosuit, as measured by UV–vis absorption at 260 nm (n = 5). (f) Representative H&E images of the bone marrow derived from mice at 1, 7, and 30 days post 5 Gy TBI with pretreatment of tFNAs, AMF, or nanosuit (Scale bars are 50 μm). (g) Representative TUNEL staining images of the bone marrow derived from mice at 7 days post 5 Gy TBI with pretreatment of tFNAs, AMF, or nanosuit (Scale bars are 20 μm). (h) Quantitative analysis of TUNEL assay indicating the percentage of TUNEL-labeled cells versus DAPI-labeled cells (n = 3). Error bars denote mean ± SEM. Statistical analysis: $*P < 0.05$, $**P < 0.01$, and $****P < 0.0001$; ns, not statistically significant. 1, Control; 2, IR; 3, tFNAs + IR; 4, AMF + IR; 5, nanosuit + IR.

2.6. No interferences of the nanosuit in tumor suppression and radiotherapeutic efficacy in Lewis lung cancer model

To explore whether the nanosuit could selectively protect the normal organs in radiotherapy, the Lewis lung cancer model, a kind of non-small cell lung cancer sensitive to radiotherapy, was introduced in the following experimental design (Fig. 6a). Besides the four irradiated groups pretreated with corresponding formulations, the saline, tFNAs, AMF, and nanosuit groups without irradiation were also included as comparisons. As the *ex vivo* tumor images (Fig. 6b) and statistics of tumor weights (Fig. 6c) shown, the tumor growths of irradiated groups were all remarkably suppressed. Importantly, no significant difference in tumor sizes between the four irradiated groups was detected, suggesting that nanosuit did not influence the efficacy of radiotherapy. The pathological appearances of tumors confirmed this conclusion (Fig. 6e). Notably, the survival analysis indicated that the 60-day survival percentage of mice in the nanosuit + IR group was the best (Fig. 6d). The high mortality in IR and tFNAs + IR group may be due to multiple organ failure during the process of ARS. The hematopoietic system and multiple organs in the nanosuit + IR group were selectively protected from IR-induced injury while the other three irradiated groups were subjected to varying degree of injuries (Fig. 6f and g). The curves in body weight changes were also consistent with above results (Fig. S22, Supporting Information). Thus, the radioprotective effect of nanosuit on normal tissues was evidently superior to AMF, in accordance with results of previous experiments performed in non-tumor-bearing mice.

Finally, the *in vivo* biosafety evaluation of nanosuit was studied. Mice were received two consecutive weeks of daily drug administration, and samples were collected. The haematological results indicated that nanosuit had no adverse effects on the main indicators (Fig. S23a, Supporting Information). There was no significant difference in body weight change between each group (Fig. S23b, Supporting Information). Therefore, the nanosuit is expected to be applied safely in future medicine.

3. Conclusion

In summary, the nanosuit was synthesized to construct a high-efficiency delivery system of AMF with the extended half-life and enhanced radioprotection capability (Fig. 7). The nanosuit was found with capability to protect DNA integrity and rescue normal cells from IR-induced death by suppressing the aberrant activation of ATM/ATR signal pathways, while not affect the efficacy of radiotherapy in cancer suppression. Pretreatment with the nanosuit reduced radiation toxicity and protected mice from lethal ARS, the nanosuit could also reverse the damages to the hematopoietic system and multi-organs in sub-lethal irradiated mice by restoring SOD activities and suppressing MDA contents. Overall, our study used nucleic acid nanomaterials to optimize the construction of competitive radioprotective strategies with high application potentials in clinics.

4. Material and methods

4.1. Synthesis and Identification of nanosuit

Four ssDNAs (Sangon Biotechnology, China) were added to TM buffer (50 mM $MgCl_2$ and 10 mM Tris-HCl, pH 8.0) in equal proportions. The mixtures were heated to 95 °C for 10 min and then 4 °C for 20 min to complete the preparation of tFNAs. Subsequently, different concentrations (40, 80, 120, 160, and 320 μM) of AMF (HY–B0639, MCE, Shanghai, China) were interfused with tFNAs (250 nM) and stirred for 6 h at room temperature. The free AMF was separated using a 30 kDa ultrafiltration tube. Encapsulation efficiency of AMF in the tFNAs was examined by high performance liquid chromatography (HPLC, Waters, China) analysis and calculated to the following formula:

$$Encapsulation\,efficiency\,(\%) = \frac{initial\,mass\,of\,AMF - residual\,mass\,of\,AMF}{initial\,mass\,of\,AMF} \times 100\%$$

To verify the successful preparation of nanosuit, the fluorescence of Gel-Red (D0139, Beyotime, China) and Hoechst 33342 (C1025, Beyotime, China) was detected via a microplate reader (Thermo Scientific, Varioskan Lux, USA). The he molecular weights of tFNA and nanosuit were measured by high performance capillary electrophoresis (HPCE, BiOptic, China). The particle sizes of tFNA and nanosuit molecule were observed by DLS (Zetasizer Nano ZS90; Malvern Instrument Ltd., UK) and TEM (Tecnai G2 F20 S-TWIN, USA) and AFM (Cypher VRS, Oxford Instruments, UK). The ζ-potential distributions of tFNA and nanosuit were analyzed by Zetasizer Nano ZS90 (Malvern Instrument Ltd., UK).

For the release assay, PBS (0.01 M, pH 7.4) or FBS (10 %, pH 7.4) was applied as release mediums. The dialysis membrane (30 kDa, Solarbio, Beijing, China) was used to divide the release medium into two compartments: the inner liquid (3 mL) and the outer fluid (30 mL). The nanosuit was dissolved in the inner liquid, and the system was incubated at 37 °C. Then quantity of AMF released into the outer fluid at different time points was measured.

4.2. Cell culture and endocytosis

BALB/3T3 clone A31 cells (ATCC, USA) were incubated in high-glucose DMEM medium (11965092, Gibco, USA) containing 10 % FBS and 1 % penicillin/streptomycin. Cells were incubated with Cy5-modified ssDNAs, tFNAs or nanosuit for 6 h and 12 h. At time points, samples were digested and centrifuged, finally detected by flow cytometer (Attune NxT, Thermo Fisher Scientific, USA) and confocal laser scanning microscope (Nikon, Japan).

4.3. Cell viability assay

To examine the effects of nanosuit on IR-induced cytotoxicity, Cell Counting Kit-8 (C0037, Beyotime, China) was applied to determine the cell viability. A31 cells were seeded into 96-well plates at 1×10^4 per well and cultured overnight. After adherent growth, A31 cells were divided into the following four groups: (i) control group; (ii) cells pretreated with tFNAs (250 nM); (iii) cells pretreated with AMF (54 μg/
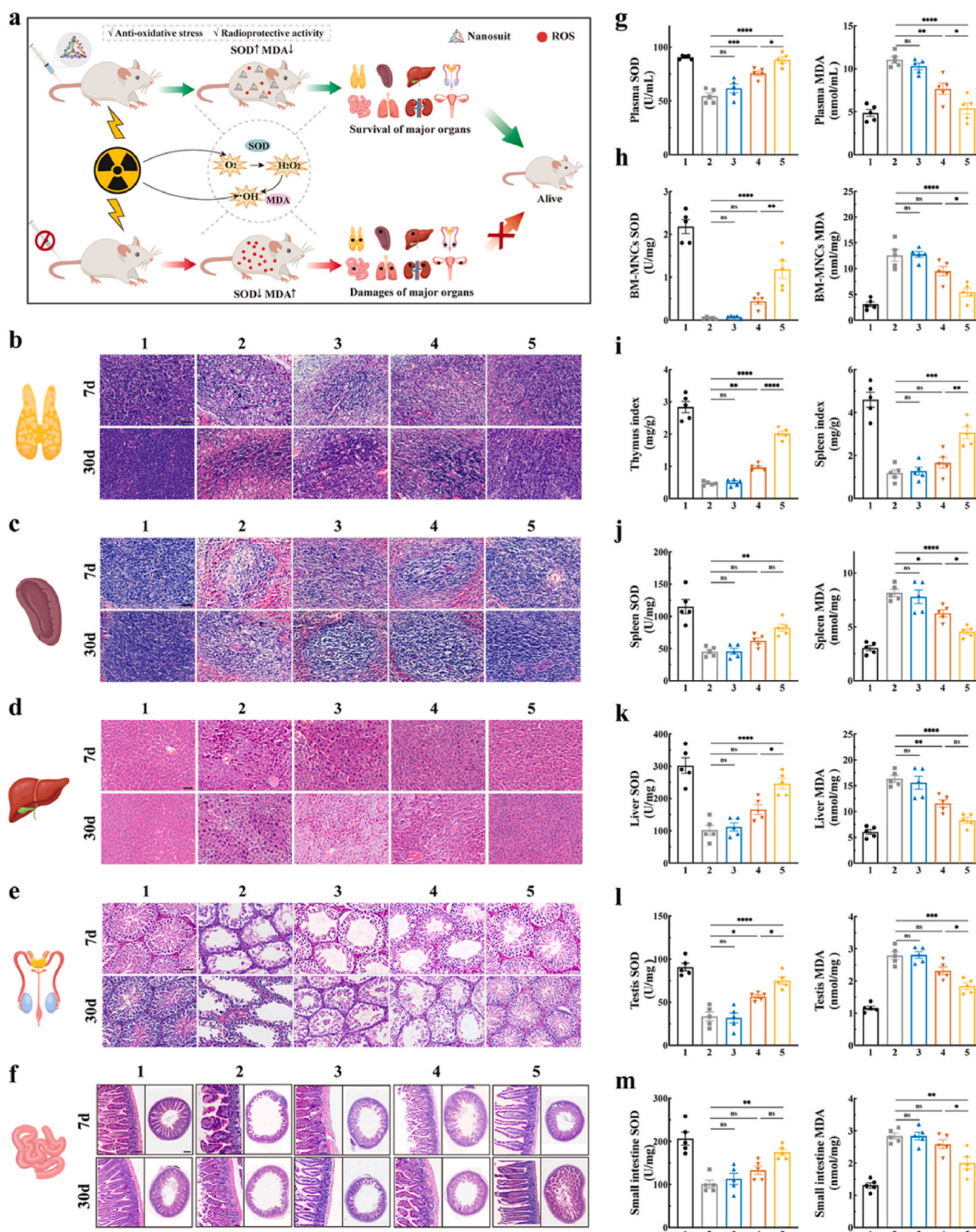
Fig. 5. Nanosuit prevented IR-induced multi-organ damage *in vivo*. (a) Schematic illustration of nanosuit preventing IR-induced multiorgan damage *in vivo* via antioxidative stress. (b–e) Representative H&E images of thymus (b), spleen (c), liver (d), and testis (e) derived from mice at 7 and 30 days post 5 Gy TBI with pretreatment of tFNAs, AMF, or nanosuit (Scale bars are 50 μm). (f) Representative H&E images of small intestine derived from mice at 7 and 30 days post 5 Gy TBI with pretreatment of tFNAs, AMF, or nanosuit (Scale bars are 100 μm in longitudinal section images, and scale bars are 300 μm in transverse section image). (g–h) SODs activities and MDA contents of plasma (g) and BM-MNCs (h) from mice at 7 days post 5 Gy TBI with pretreatment of tFNAs, AMF, or nanosuit (n = 5). (i) Thymus and spleen index of mice at 7 days post 5 Gy TBI with pretreatment of tFNAs, AMF, or nanosuit (n = 5). (j–m) SODs activities and MDA contents of spleen (j), liver (k) and testis (l) and small intestine (m) from mice at 7 days post 5 Gy TBI with pretreatment of tFNAs, AMF, or nanosuit (n = 5). Error bars denote mean ± SEM. Statistical analysis: *$P < 0.05$, **$P < 0.01$, ***$P < 0.001$, and ****$P < 0.0001$; ns, not statistically significant. 1, Control; 2, IR; 3, tFNAs + IR; 4, AMF + IR; 5, nanosuit + IR.
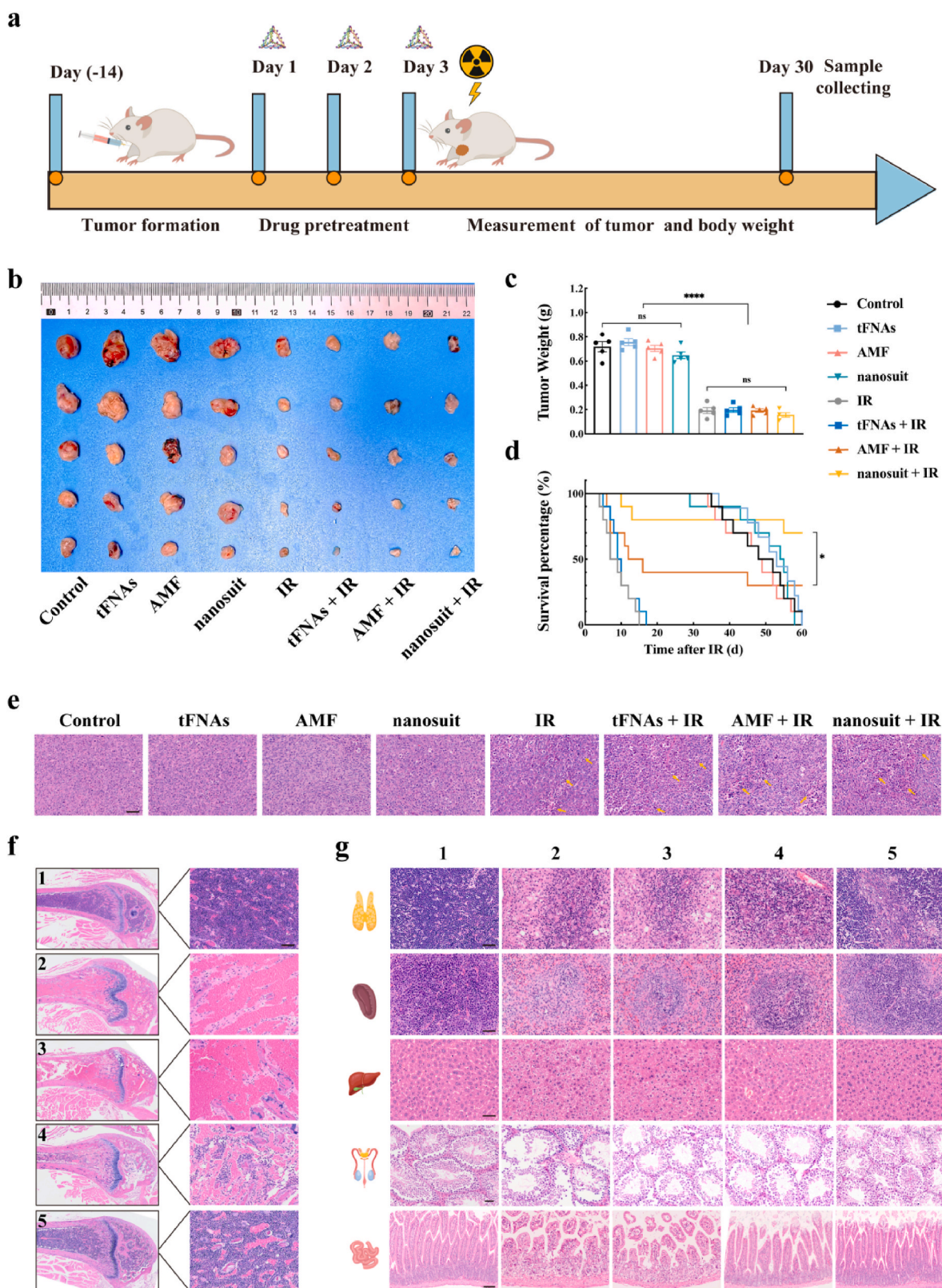
Fig. 6. Nanosuit showed no interferences of tumor suppression with radiotherapeutic efficacy in Lewis lung cancer model. (a) Schematic illustration of the experiment procedure. Photographs (b) and tumor weights (c) of tumors excised from tumor-bearing mice at 30 days after 5Gy (n = 5). (d) Survival analysis using Kaplan-Meier methods indicated the 60-day survival percentage of tumor-bearing mice after 6.5Gy. (n = 10). (e) Representative H&E images of tumors at 30 days after 5Gy (Scale bars are 50 μm). (f) Representative H&E images of the bone marrow derived from tumor-bearing mice at 30 days after 5Gy (Scale bars are 50 μm). (g) Representative H&E images of thymus, spleen, liver, testis, and small intestine derived from tumor-bearing mice at 30 days after 5Gy (Scale bars are 100 μm in longitudinal section images and 50 μm in other images). Error bars denote mean ± SEM. Statistical analysis: *P < 0.05 and ****P < 0.0001; ns, not statistically significant. 1, Control; 2, IR; 3, tFNAs + IR; 4, AMF + IR; 5, nanosuit + IR.
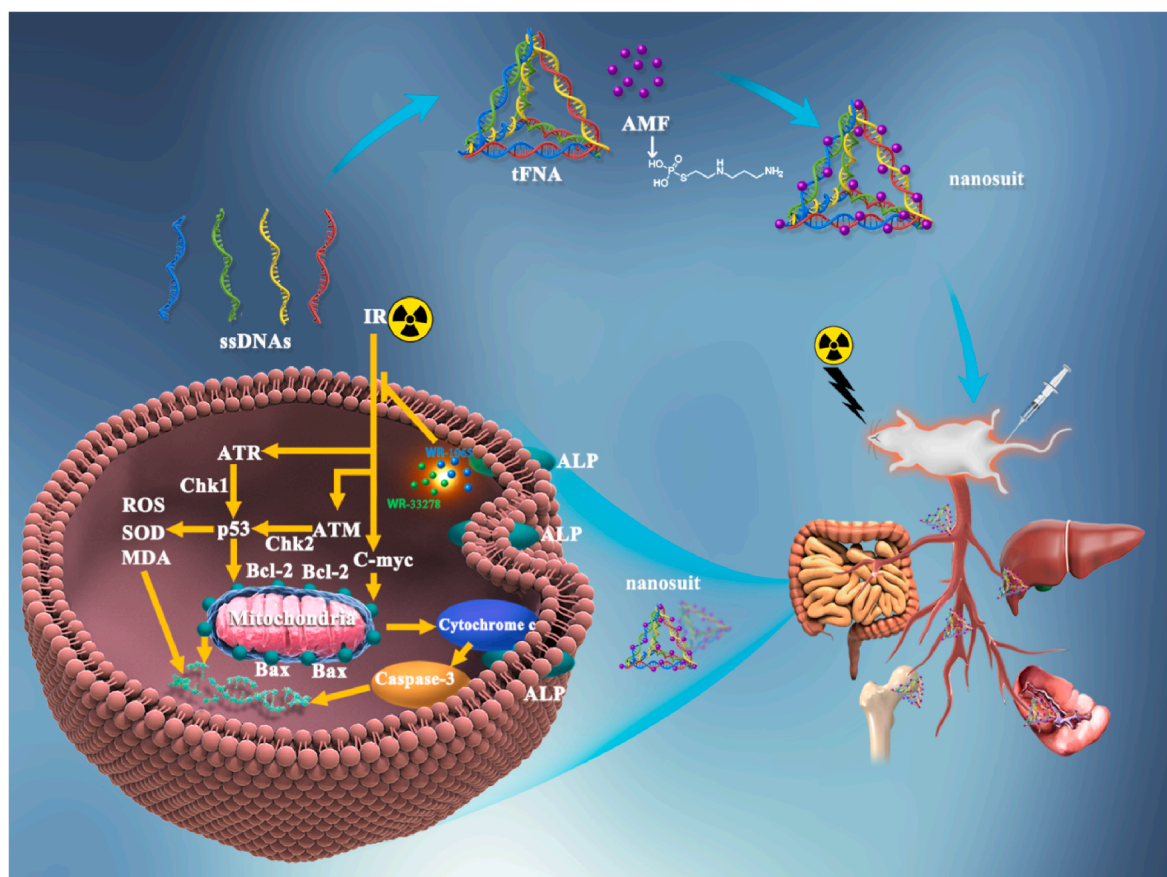
Fig. 7. The four specific ssDNAs are assembled into three-dimensional polyhedron tFNAs, and then nanosuit (tFNAs@AMF) is formed by co-incubation of tFNAs and AMF, to construct a high-efficiency delivery system of AMF with the extended half-life and enhanced radioprotection capability. Upon IR exposure, the nanosuit can suppress the aberrant activation of ATM/ATR signaling pathway, thereby regulating the molecular markers of anti-apoptosis, anti-oxidative stress, and eventually blocking DNA breakage in normal cells. Finally, the enhanced prevention of IR-induced multi-organ damage is achieved.

mL); and (iv) cells pretreated with nanosuit (250 nM) for 12 h. At time point, the four groups were exposed to 0, 2, 4, 8, or 10 Gy radiations (RS2000Prox, Rad Source, USA), respectively. After 12 h, the absorbance of samples was measured at 450 nm via a microplate reader (Thermo Scientific, Varioskan Lux, USA). The dose of 6 Gy was selected. The mouse Lewis lung cancer cells (ATCC, USA) were cultured and measured in the same way.

4.4. ROS detection

Based on cell viability assay, A31 cells were pretreated with tFNAs, AMF or nanosuit for 12 h and then exposed to 6 Gy radiation. After 12 h incubation, the ROS Assay Kit (S0033S, Beyotime, China) was used to measure ROS levels intracellularly. Cells were loaded with the probe of DCFH-DA (1:1000) and incubated for 20 min at 37 °C. Finally, images were captured performing a confocal laser scanning microscope (Nikon, Japan).

4.5. Apoptosis detection

Apoptosis-related proteins were detected by immunofluorescence staining. The samples were fixed by 4 % paraformaldehyde solution (FB002, Gibco, USA) for 15–20 min, 0.3 % Triton X-100 (HFH10, Gibco, USA) for 10 min and 5 % goat serum (35-076-CV, Corning, USA) for 1 h. Then samples were immersed in the corresponding diluted antibodies overnight at 4 °C. Primary antibodies against Caspase-3 (ab13847, 1:200) and Bcl-2 (ab196495, 1:200) were acquired from Abcam (Cambridge, U.K.). Primary antibodies against Bax (#2772, 1:350) and

Cytochrome *c* (#12963, 1:300) were acquired from Cell Signaling Technology (Danvers, USA). Next, samples were rewarmed and incubated in secondary antibodies (A0468 and A0473, Beyotime, China) for 1 h at 37 °C. Phalloidin-FITC and DAPI (P5282 and 10236276001, Sigma, USA) were stained to delineate the cytoskeleton and nucleus. For the TUNEL assay, One Step TUNEL Apoptosis Assay Kit (C1086, Beyotime, China) was applied to measure cell apoptosis. At last, immunofluorescence images were visualized by a confocal laser scanning microscope.

4.6. Detection of DNA damage

Comet assay was performed to evaluate DNA damages. 180 μL of normal melting point agarose (Hispanagar S.A., Spain) at 1 % was paved homogeneously on preheated glass slides. After cooled down and solidified, 100 μL of cell suspension was interfused with 150 μL of low-melting-point agarose (0.8 %). Subsequently, the mixture was dropped onto the first layer of agarose gel completely. After solidification again, 100 μL of low-melting-point agarose (0.5 %) was rapidly dropped to the second layer of agarose gel. Then the solidified slides were immersed in freshly-prepared lysis buffer (4 °C) for 2 h, followed by immersing them in electrophoresis buffer for 30 min. Electrophoresis was performed at 25 V and 300 mA for 15 min. Finally, the slides were neutralized with neutralization buffer for 30 min and stained with ethidium bromide (E7637, Sigma, USA) for 10 min. The DNA damage degree was analyzed by Comet Assay Software Pect (CASP 1.2.3 beta 1) at last. The foci expression of γ-H2A.X was observed by DNA Damage Assay Kit by γ-H2A.X Immunofluorescence (C2035S, Beyotime, China). The

expression of DNA-PKcs was observed by immunofluorescence staining. Antibodies against DNA-PKcs (ab44815, 1:100) were acquired from Abcam (Cambridge, U.K.).

4.7. Western blot

Total cell protein samples were obtained via a Total Protein Extraction Kit (KGB5303, Keygen Biotech, China). Samples were mixed with 5 × loading buffer at a ratio of 4:1 before boiled at 100 °C for 5–10 min. The separation of target markers into corresponding molecular weight albumens was performed by SDS-PAGE gels (8–12 %). After transferred onto polyvinylidene fluoride (PVDF) membranes (Bio-Rad, USA), they were exposed to QuickBlock™ Western (P0242, Beyotime, China) for 15 min, followed by incubated in primary antibodies overnight at 4 °C. Antibodies against GAPDH (ab8245, 1:1000), Caspase-3 (ab13847, 1:500), Bcl-2 (ab196495, 1:1000), γ-H2A.X (ab81299, 1:5000), DNA-PKcs (ab44815, 1:1000), ATM (ab199726, 1:1000), ATR (ab2905, 1:1000), C-myc (ab78318, 1:1000), p53 (ab90363, 1:1000) were purchased from Abcam. Antibodies against Bax (#2772, 1:1000), Cytochrome c (#12963, 1:1000), Chk1 (#2360, 1:1000), Chk2 (#2662, 1:1000) were acquired from Cell Signaling Technology. Next day, the membranes were immersed in secondary antibodies (A0208 and A0216, Beyotime, China) solution for 1 h after rewarmed. At last, the bands of target markers were visualized by the enhanced chemiluminescence (ECL) detection system (Bio-Rad, USA) and analyzed by Image J 1.53c.

4.8. Animal model

All animal experimental procedures were in compliance with ethical criterion of Sichuan University. BALB/C mice (6–8 weeks, 18–22 g) were obtained from Ensiweier (Chengdu, China) and kept on a 12:12 h light-dark cycle for one full week to adapt to new environment. Mice were randomly divided into two large groups: receiving sub-lethal radiation (5 Gy) and lethal radiation (6.5 Gy). RS2000 (Rad Source, Atlanta, USA) was applied for radiation. Each large group was further divided into five small groups: (i) control group; (ii) IR group; (iii) tFNAs pre-treatment + IR group; (iv) AMF pre-treatment + IR group; (v) nanosuit pre-treatment + IR group. At the beginning, mice received 200 μL intravenous (i. v.) injection of corresponding drugs every day. The pretreatment lasted for 3 days before IR. All the 6.5 Gy TBI mice were monitored for survival amount within 30 days.

4.9. Biodistribution

For organ biodistribution, mice were euthanized at different times post injection of tFNAs or nanosuit (15, 30, 60, and 120 min), and major organs (heart, liver, spleen, lung, and kidney) were derived and analyzed by whole-body fluorescent system (IVIS Lumina III Series, PerkinElmer, USA). In the same way, tumors and major organs derived from tumor-bearing mice at different times (3 times administration (qd), 15 min, 45 min, 1.5 h, 3 h, 6 h, 12 h, and 24 h) were detected.

4.10. Pharmacokinetics experiment

Pharmacokinetics experiment was performed to investigate the blood metabolism of tFNAs, AMF or nanosuit. TFNAs, AMF or nanosuit was labeled by Cy5, separately. The blood samples were collected via the tail tip of the mice after injection from 15 min to 12 h. Finally, the blood samples were detected using the channel of Cy5 fluorescence of Gel & Blot Imaging system (ChemiDoc MP, Bio-Rad, USA). Pharmacokinetics was analyzed via the mean fluorescence intensity of the blood samples.

4.11. Hematology and histological examination

At the time points of 1 day, 7 days, and 30 days post 5 Gy TBI, mice were anesthetized and the blood samples were extracted via orbital vein.

The hematological parameters including WBC, RBC, PLT, ALT, and AST were analyzed by a blood cell analyzer (BC-2800Vet, Mindray, China). The plasma SOD activities (A001, Institute of Biological Engineering of Nanjing Jianchen, China) and MDA contents (A003, Institute of Biological Engineering of Nanjing Jianchen, China) were analyzed according to the kit instructions. Thymus index and spleen index were measured by weighing. For histological examination, major organs (heart, liver, spleen, lung, kidney, bone marrow, thymus, testis, and small intestine) were separated, fixed in paraformaldehyde solution (4 %), and then dehydrated, paraffin-embedded and sliced into 4 μm thick sections. Hematoxylin-eosin (H&E) staining was performed on the tissue slides, which was imaged by Vectra Polaris quantitative slide scanner (PerkinElmer, USA) and VS200 slide scanner (Olympus, USA). For the TUNEL assay, the bone tissues were fixed and incubated in a permeabilization solution. Subsequently, TUNEL Cell Apoptosis Detection Kit (CF488, Servicebio, China) was applied to evaluate apoptosis in bone tissues. Images were captured via a laser confocal microscope (Nikon, Japan). Bone marrow cells were flushed and isolated into BM-MNCs using a BM-MNCs extraction kit (P9600, Solarbio, China). In addition, major organs were harvested and centrifugated, in order that the supernatant could be collected for detecting SOD activities and MDA contents.

4.12. Exploration of therapeutic potential

To confirm whether the nanosuit could exhibit therapeutic potential in irradiated lesions, mice were randomly divided into two large groups as before: receiving sub-lethal radiation (5 Gy) and lethal radiation (6.5 Gy). Each large group was further divided into five small treatment groups: (i) control group; (ii) IR group; (iii) IR + tFNAs treatment group; (iv) IR + AMF treatment group; (v) IR + nanosuit treatment group. At the beginning, mice were irradiated at the corresponding doses, and then received 200 μL intravenous (i.v.) injection of different drugs for three consecutive days. All the 6.5 Gy TBI mice were monitored for survival amount within 30 days. At time point, all the 5 Gy TBI mice were euthanized, the blood samples were extracted via orbital vein, and major organs (bone marrow, spleen, thymus, testis, and small intestine) were collected for further analysis.

4.13. The Lewis lung cancer model

Mouse Lewis lung cancer cells were suspended in 100 μL growth medium (at the concentration of 1×10^7 cells in 1 mL) and subcutaneously injected into the underarm of 4-week-old male BALB/C mice. After 14 days, the length of tumors reached about 3–5 mm, and the mice were randomly divided into two large groups as before: receiving sub-lethal radiation (5 Gy) and lethal radiation (6.5 Gy). Each large group was further divided into eight small treatment groups: (i) control group; (ii) tFNAs group; (iii) AMF group; (iv) nanosuit group; (v) IR group; (vi) tFNAs pre-treatment + IR group; (vii) AMF pre-treatment + IR group; (viii) nanosuit pre-treatment + IR group. Corresponding drugs were given via the tail vein for three consecutive days as above. And then the four groups of them received radiation (5 Gy or 6.5 Gy). The tumor volume and body weight of 5 Gy mice were monitored for 30 days. At time point, all mice were euthanized, tumors were collected and weighted, and major organs (bone marrow, spleen, thymus, testis, and small intestine) were collected for further analysis. All the 6.5 Gy mice were monitored for survival amount within 60 days.

4.14. Safety assessment

To assess the drug safety, 6-week-old male BALB/C mice were given two consecutive weeks of daily drug administration. The body weight of mice was recorded. Finally, the mice were euthanized, and the blood was collected for the hematological examinations.

4.15. Statistical analysis

Error bars denote means of at least three independent experiments ± standard error of the mean (SEM). Multiple group comparisons of data were calculated by a one-way analysis of variance (ANOVA) or two-way ANOVA with GraphPad Prism v8.2.1 software. The statistical significance was indicated as $*P < 0.05$, $**P < 0.01$, $***P < 0.001$, and $****P < 0.0001$; ns, not statistically significant.

Ethics approval and consent to participate

All animal experiments were approved by the Ethics Committee of West China Hospital of Stomatology, Sichuan University with an approval number: WCHSIRB-D-2019-100.

CRediT authorship contribution statement

Yuting Yang: Formal analysis, Data curation, Conceptualization. **Jinlong Yang:** Formal analysis, Data curation. **Jianwei Zhu:** Data curation. **Xingyu Chen:** Formal analysis. **Li Zhou:** Formal analysis. **Wenjuan Ma:** Data curation, Conceptualization. **Yunfeng Lin:** Writing – review & editing, Supervision, Funding acquisition, Conceptualization.

Declaration of competing interest

The authors declare that they have no known competing financial interests or personal relationships that could have appeared to influence the work reported in this paper.

Acknowledgments

Appendix A. Supplementary data

Supplementary data to this article can be found online at https://doi.org/10.1016/j.bioactmat.2024.05.017.

References

[1] J. Xie, C. Wang, F. Zhao, Z. Gu, Y. Zhao, Application of multifunctional nanomaterials in radioprotection of healthy tissues, Adv. Healthcare Mater. 7 (2018) 1800421, https://doi.org/10.1002/adhm.201800421.

[2] K. Leuraud, D.B. Richardson, E. Cardis, R.D. Daniels, M. Gillies, J.A. O'Hagan, G. B. Hamra, R. Haylock, D. Laurier, M. Moissonnier, M.K. Schubauer-Berigan, I. Thierry-Chef, A. Kesminiene, Ionising radiation and risk of death from leukaemia and lymphoma in radiation-monitored workers (INWORKS): an international cohort study, Lancet Haematol 2 (7) (2015) e276–e281, https://doi.org/10.1016/S2352-3026(15)00094-0.

[3] C. Allen, S. Her, D.A. Jaffray, Radiotherapy for cancer: present and future, Adv. Drug Deliv. Rev. 109 (2017) 1–2, https://doi.org/10.1016/j.addr.2017.01.004.

[4] J.C. Teepen, R.E. Curtis, G.M. Dores, A. Berrington De Gonzalez, M.M. van den Heuvel-Eibrink, L.C.M. Kremer, E.S. Gilbert, F.E. van Leeuwen, C.M. Ronckers, L. M. Morton, Risk of subsequent myeloid neoplasms after radiotherapy treatment for a solid cancer among adults in the United States, 2000-2014, Leukemia 32 (12) (2018) 2580–2589, https://doi.org/10.1038/s41375-018-0149-2.

[5] K.R. Brown, E. Rzucidlo, J. Vascul, Acute and chronic radiation injury, J. Vasc. Surg. 53 (1 Suppl) (2011) 15S–21S, https://doi.org/10.1016/j.jvs.2010.06.175.

[6] B. Hu, C. Jin, H.B. Li, The DNA-sensing AIM2 inflammasome controls radiation-induced cell death and tissue injury, Science 354 (6313) (2016) 765–768, https://doi.org/10.1126/science.aaf7532.

[7] S. Siva, M.P. MacManus, R.F. Martin, O.A. Martin, Abscopal effects of radiation therapy: a clinical review for the radiobiologist, Cancer Lett. 356 (1) (2015) 82–90, https://doi.org/10.1016/j.canlet.2013.09.018.

[8] S.M. Bentzen, Preventing or reducing late side effects of radiation therapy: radiobiology meets molecular pathology, Nat. Rev. Cancer 6 (9) (2006) 702–713, https://doi.org/10.1038/nrc1950.

[9] J. Falck, J. Coates, S. Jackson, Conserved modes of recruitment of ATM, ATR and DNA-PKcs to sites of DNA damage, Nature 434 (7033) (2005) 605–611, https://doi.org/10.1038/nature03442.

[10] D. Menolfi, S. Zha, ATM, ATR and DNA-PKcs kinases-the lessons from the mouse models: inhibition≠deletion, Cell Biosci. 10 (2020) 8, https://doi.org/10.1186/s13578-020-0376-x.

[11] S. He, N.E. Sharpless, Senescence in health and disease, Cell 169 (6) (2017) 1000–1011, https://doi.org/10.1016/j.cell.2017.05.015.

[12] L. Wang, L. Lankhorst, R. Bernards, Exploiting senescence for the treatment of cancer, Nat. Rev. Cancer 22 (6) (2022) 340–355, https://doi.org/10.1038/s41568-022-00450-9.

[13] L.G. Burdelya, V.I. Krivokrysenko, T.C. Tallant, An agonist of toll-like receptor 5 has radioprotective activity in mouse and primate models, Science 320 (5873) (2008) 226–230, https://doi.org/10.1126/science.1154986.

[14] R.M. Johnke, J.A. Sattler, R.R. Allison, Radioprotective agents for radiation therapy: future trends, Future Oncol. 10 (15) (2014) 2345–2357, https://doi.org/10.2217/fon.14.175.

[15] E. Obrador, R. Salvador, J.I. Villaescusa, Radioprotection and radiomitigation: from the bench to clinical practice, Biomedicines 8 (11) (2020) 461, https://doi.org/10.3390/biomedicines8110461.

[16] K.N. Mishra, B.A. Moftah, G.A. Alsbeih, Appraisal of mechanisms of radioprotection and therapeutic approaches of radiation countermeasures, Biomed. Pharmacother. 106 (2018) 610–617, https://doi.org/10.1016/j.biopha.2018.06.150.

[17] J.R. Kouvaris, V.E. Kouloulias, L.J. Vlahos, Amifostine: the first selective-target and broad-spectrum radioprotector, Oncol. 12 (6) (2007) 738–747, https://doi.org/10.1634/theoncologist.12-6-738.

[18] M. King, Use of amifostine for cytoprotection during radiation therapy: a review, Oncology 98 (2) (2020) 61–80, https://doi.org/10.1159/000502979.

[19] M. Hofer, Two new faces of amifostine: protector from DNA damage in normal cells and inhibitor of DNA repair in cancer cells, J. Med. Chem. 59 (7) (2016) 3003–3017, https://doi.org/10.1021/acs.jmedchem.5b01628.

[20] M.L. Hensley, American society of clinical oncology 2008 clinical practice guideline update summary: use of chemotherapy and radiation therapy protectants, J. Oncol. Pract. 4 (6) (2008) 277–279, https://doi.org/10.1200/JOP.0868502.

[21] V.K. Singh, T.M. Seed, The efficacy and safety of amifostine for the acute radiation syndrome, Expet Opin. Drug Saf. 18 (11) (2019) 1077–1090, https://doi.org/10.1080/14740338.2019.1666104.

[22] N.P. Praetorius, T.K. Mandal, Alternate delivery route for amifostine as a radio-/chemo-protecting agent, J. Pharm. Pharmacol. 60 (7) (2008) 809–815, https://doi.org/10.1211/jpp.60.7.0001.

[23] T. Tian, T. Zhang, S. Shi, Y. Gao, X. Cai, Y. Lin, A dynamic DNA tetrahedron framework for active targeting, Nat. Protoc. 18 (4) (2023) 1028–1055, https://doi.org/10.1038/s41596-022-00791-7.

[24] W. Ma, Y. Yang, J. Zhu, W. Jia, T. Zhang, Z. Liu, X. Chen, Y. Lin, Biomimetic nanoerythrosome-coated aptamer-DNA tetrahedron/maytansine conjugates: pH-responsive and targeted cytotoxicity for HER2-positive breast cancer, Adv. Mater. 34 (46) (2022) e2109609, https://doi.org/10.1002/adma.202109609.

[25] J. Li, Y. Yao, Y. Wang, J. Xu, D. Zhao, M. Liu, S. Shi, Y. Lin, Modulation of the crosstalk between Schwann cells and macrophages for nerve regeneration: a therapeutic strategy based on a multifunctional tetrahedral framework nucleic acids system, Adv. Mater. 34 (46) (2022) e2202513, https://doi.org/10.1002/adma.202202513.

[26] Y. Li, Z. Cai, W. Ma, L. Bai, E. Luo, Y. Lin, A DNA tetrahedron-based ferroptosis-suppressing nanoparticle: superior delivery of curcumin and alleviation of diabetic osteoporosis, Bone Res. 12 (1) (2024) 14, https://doi.org/10.1038/s41413-024-00319-7.

[27] C. Qi, Q. Sun, D. Xiao, M. Zhang, S. Gao, B. Guo, Y. Lin, Tetrahedral framework nucleic acids/hyaluronic acid-methacrylic anhydride hybrid hydrogel with antimicrobial and anti-inflammatory properties for infected wound healing, Int. J. Oral Sci. 16 (1) (2024) 30, https://doi.org/10.1038/s41368-024-00290-3.

[28] J. Sun, Y. Gao, Y. Yao, Y. Li, M. Feng, L. Bai, X. Chen, Y. Ge, Y. Lin, X. Cai, Bone tissue engineering based on sustained release of MiR29c-modified framework nucleic acids from an injectable hydrogel, Chem. Eng. J. 487 (2024) 150706, https://doi.org/10.1016/j.cej.2024.150706.

[29] Y. Chen, X. Chen, B. Zhang, Y. Zhang, S. Li, Z. Liu, Y. Gao, Y. Zhao, L. Yan, Y. Li, T. Tian, Y. Lin, DNA framework signal amplification platform-based high-throughput systemic immune monitoring, Signal Transduct. Targeted Ther. 9 (1) (2024) 28, https://doi.org/10.1038/s41392-024-01736-0.

[30] M. Zhang, Y. Wen, Z. Huang, X. Qin, M. Zhou, D. Xiao, W. Cui, Z. Liu, Y. Lin, Targeted therapy for autoimmune diseases based on multifunctional frame nucleic acid system: blocking TNF-α-NF-κB signaling and mediating macrophage polarization, Chem. Eng. J. 454 (2023) 140399, https://doi.org/10.1016/j.cej.2022.140399.

[31] T. Zhang, H. Ma, X. Zhang, S. Shi, Y. Lin, Functionalized DNA nanomaterials targeting toll-like receptor 4 prevent bisphosphonate-related osteonecrosis of the

jaw via regulating mitochondrial homeostasis in macrophages, Adv. Funct. Mater. 33 (15) (2023) 2213401, https://doi.org/10.1002/adfm.202213401.

[32] S. Shi, T. Chen, W. Lu, Y. Chen, D. Xiao, Y. Lin, Amelioration of osteoarthritis via tetrahedral framework nucleic acids delivering microRNA-124 for cartilage regeneration, Adv. Funct. Mater. (2023) 202305558, https://doi.org/10.1002/adfm.202305558.

[33] Y. Xie, J. He, S. Li, X. Chen, T. Zhang, Y. Zhao, Y. Lin, X. Cai, A transdermal drug delivery system based on nucleic acid nanomaterials for skin photodamage treatment, Adv. Funct. Mater. (2023) 202303580, https://doi.org/10.1002/adfm.202303580.

[34] Y. Zhao, S. Li, M. Feng, M. Zhang, Z. Liu, Y. Yao, T. Zhang, Y. Jiang, Y. Lin, X. Cai, Effects of puerarin-loaded tetrahedral framework nucleic acids on osteonecrosis of the femoral head, Small (2023) e2302326, https://doi.org/10.1002/smll.202302326.

[35] L. Yao, J. Li, X. Qin, Z. Liu, Y. Jiang, T. Zhang, Y. Lin, Anti-fibrotic and antioxidant effects of a tetrahedral framework nucleic acid-based chlorogenic acid delivery system, ACS Mater. Lett. 5 (2023) 1153–1163, https://doi.org/10.1021/acsmaterialslett.2c00839.

[36] T. Zhang, T. Tian, Y. Lin, Functionalizing framework nucleic-acid-based nanostructures for biomedical application, Adv. Mater. 34 (46) (2022) e2107820, https://doi.org/10.1002/adma.202107820.

[37] J. Zhu, Y. Yang, W. Ma, Y. Wang, L. Chen, H. Xiong, C. Yin, Z. He, W. Fu, R. Xu, Y. Lin, Antiepilepticus effects of tetrahedral framework nucleic acid via inhibition of gliosis-induced downregulation of glutamine synthetase and increased AMPAR internalization in the postsynaptic membrane, Nano Lett. 22 (6) (2022) 2381–2390, https://doi.org/10.1021/acs.nanolett.2c00025.

[38] H. Wang, J. Gong, W. Chen, Q. Sun, T. Zhang, Y. Lin, X. Cai, Tetrahedral framework nucleic acids' role in facilitating chronic diabetic wound repair via the endoplasmic reticulum-mitochondrial pathway, Nano Today 56 (2024) 102252, https://doi.org/10.1016/j.nantod.2024.102252.

[39] R. Yan, W. Cui, W. Ma, J. Li, Z. Liu, Y. Lin, Typhaneoside-tetrahedral framework nucleic acids system: mitochondrial recovery and antioxidation for acute kidney injury treatment, ACS Nano 17 (9) (2023) 8767–8781, https://doi.org/10.1021/acsnano.3c02102.

[40] X. Ren, M. Huo, M. Wang, H. Lin, X. Zhang, J. Yin, Y. Chen, H. Chen, Highly catalytic niobium carbide (MXene) promotes hematopoietic recovery after radiation by free radical scavenging, ACS Nano 13 (6) (2019) 6438–6454, https://doi.org/10.1021/acsnano.8b09327.

[41] G.K. Atkin-Smith, R. Tixeira, S. Paone, S. Mathivanan, C. Collins, M. Liem, K. J. Goodall, K.S. Ravichandran, M.D. Hulett, I.K. Poon, A novel mechanism of generating extracellular vesicles during apoptosis via a beads-on-a-string membrane structure, Nat. Commun. 6 (2015) 7439, https://doi.org/10.1038/ncomms8439.

[42] E. Velardi, J.J. Tsai, S. Radtke, K. Cooper, K.V. Argyropoulos, S. Jae-Hung, L. F. Young, A. Lazrak, O.M. Smith, S. Lieberman, F. Kreines, Y. Shono, T. Wertheimer, R.R. Jenq, A.M. Hanash, P. Narayan, Z. Lei, M.A. Moore, H.P. Kiem, Suppression of luteinizing hormone enhances HSC recovery after hematopoietic injury, Nat. Med. 24 (4) (2018) 239–246, https://doi.org/10.1038/nm.4470.

[43] H. Liang, C. Xu, D. Guo, F. Peng, N. Chen, H. Song, X. Ji, Dismantlable coronated nanoparticles for coupling the induction and perception of immunogenic cell death, Adv. Mater. (2024) e2313097. http://doi:10.1002/adma.202313097.

[44] D. Zhang, D. Zhong, O. Jiang, J. He, Y. Qi, W. Chen, X. Zhang, W. Tao, M. Zhou, Microalgae-based oral microcarriers for gut microbiota homeostasis and intestinal protection in cancer radiotherapy, Nat. Commun. 13 (1) (2022) 1413, https://doi.org/10.1038/s41467-022-28744-4.

[45] A.M. Pisoschi, A. Pop, The role of antioxidants in the chemistry of oxidative stress: a review, Eur. J. Med. Chem. 97 (2015) 55–74, https://doi.org/10.1016/j.ejmech.2015.04.040.

[46] F. Cruz-Guilloty, V.L. Perez, Molecular medicine: defence against oxidative damage, Nature 478 (7367) (2011) 42–43, https://doi.org/10.1038/478042a.